Complete Analytical Solution of Electromagnetic Field Problem of High-Speed Spinning Ball

T. Reichert
T. Nussbaumer
J. W. Kolar

Complete analytical solution of electromagnetic field problem of high-speed spinning ball

T. Reichert, T. Nussbaumer, and J. W. Kolar

Related Articles

A simple maximum power point tracking based control strategy applied to a variable speed squirrel cage induction generator
J. Renewable Sustainable Energy 4, 053124 (2012)

Dynamic optimization of the tracking system for a pseudo-azimuthal photovoltaic platform
J. Renewable Sustainable Energy 4, 053117 (2012)

Control strategies of doubly fed induction generator-based wind turbine system with new rotor current protection topology
J. Renewable Sustainable Energy 4, 043123 (2012)

A high-temperature double-mode piezoelectric ultrasonic linear motor
Appl. Phys. Lett. 101, 072902 (2012)

Note: Design of a novel rotating magnetic field device
Rev. Sci. Instrum. 83, 066109 (2012)

Additional information on J. Appl. Phys.

Journal Homepage: http://jap.aip.org/

Journal Information: http://jap.aip.org/about/about_the_journal

Top downloads: http://jap.aip.org/features/most_downloaded

Information for Authors: http://jap.aip.org/authors
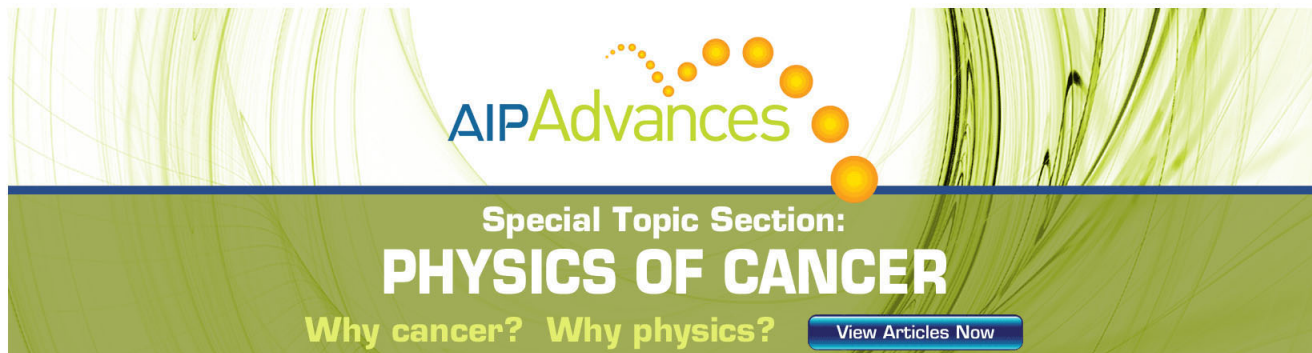
Complete analytical solution of electromagnetic field problem of high-speed spinning ball

T. Reichert,[1] T. Nussbaumer,[2] and J. W. Kolar[1]

[1]*Power Electronic Systems Laboratory, ETH Zurich, Zurich 8092, Switzerland*
[2]*Levitronix GmbH, Technoparkstrasse 1, Zurich 8005, Switzerland*

In this article, a small sphere spinning in a rotating magnetic field is analyzed in terms of the resulting magnetic flux density distribution and the current density distribution inside the ball. From these densities, the motor torque and the eddy current losses can be calculated. An analytical model is derived, and its results are compared to a 3D finite element analysis. The model gives insight into the torque and loss characteristics of a solid rotor induction machine setup, which aims at rotating the sphere beyond 25 Mrpm. © 2012 American Institute of Physics. [http://dx.doi.org/10.1063/1.4765676]

I. INTRODUCTION

The current world record for the rotational speed of a small spinning ball was achieved by Beams as early as the year 1946. He succeeded in rotating a steel sphere of 0.8 mm in diameter with a speed of 23.16 Mrpm.[1] Since then, no successful attempt has been reported that would even come close to that record (not considering setups in the microscopic scale, e.g., Ref. [2]). A new project at ETH Zurich aims at achieving high rotational speeds in the tens of millions rpm range with the ultimate goal of outperforming the long standing record by Beams. For the setup, a small steel ball, which is placed in a vacuum tube, is levitated through magnetic forces and accelerated with a radial coil system. Different possible bearing and drive setups have already been presented recently.[3,4] The first tests revealed that air coils should be employed for the drive in order to avoid heavy iron losses. As a consequence, the external magnetic flux density generated with the coil system is largely reduced to around 10 mT.

In this article, the electromagnetic characteristics of such a so-called solid rotor induction machine[5–7] are analyzed in great detail. In Sec. II, the field problem is stated, derived from basic equations and boundary conditions. This allows calculating the vector potential, from which both the magnetic flux density and the current density due to eddy currents can easily be determined. From these field quantities, the integral values for the motor torque and the eddy current losses can be found. A comparison with a 3D finite element analysis is undertaken in Sec. III in order to confirm the theoretical results. Additionally, a graphical comparison between plots resulting from both the simulation and from the formulas proves the validity of the theoretical model.

II. ANALYTICAL ANALYSIS OF ELECTROMAGNETIC FIELD PROBLEM

For the following calculations, three different coordinate systems are introduced. A Cartesian coordinate system fixed in space builds the reference frame, with its origin in the middle of the spinning ball and its unity vector given by $(\vec{e}_x \quad \vec{e}_y \quad \vec{e}_z)^{\mathrm{T}}$. Additionally, the *z*-axis corresponds with the axis of rotation. A second Cartesian coordinate system is fixed with the spinning ball and rotates with its current speed in relation to the reference frame. The unity vector is expressed with $(\vec{e}_1 \quad \vec{e}_2 \quad \vec{e}_z)^{\mathrm{T}}$, where $\vec{e}_z$ is identical for both coordinate systems (see Fig. 1). Finally, a spherical coordinate system $(\vec{e}_r \quad \vec{e}_\theta \quad \vec{e}_\varphi)^{\mathrm{T}}$ is introduced as well, which is derived from the rotating Cartesian coordinate system.

The electromagnetic field problem can be simplified with a trick, as in the end only the frequency difference between the rotating magnetic field and the spinning ball is of interest (the so-called slip frequency according to the working principle of induction machines). For that purpose, a fixed magnetic flux density $\vec{B}_0$ into the positive *x*-direction is set, given by

$$\vec{B}_0 = B_0 \, \vec{e}_x. \tag{1}$$

The rotational speed of the spinning ball is then set to the aforementioned frequency difference (slip frequency), denoted with ω. In order to carry out the calculations in the rotating reference frame, the magnetic flux density is transformed, using the vector

$$\vec{b} = \underbrace{\begin{pmatrix} 1 \\ j \\ 0 \end{pmatrix} \cdot \begin{pmatrix} \vec{e}_x \\ \vec{e}_y \\ \vec{e}_z \end{pmatrix} e^{-j\omega t}}_{\vec{c}} = \begin{pmatrix} 1 \\ j \\ 0 \end{pmatrix} \cdot \begin{pmatrix} \vec{e}_1 \\ \vec{e}_2 \\ \vec{e}_z \end{pmatrix}$$

$$= \begin{pmatrix} \sin\theta(\cos\varphi + j\sin\varphi) \\ \cos\theta(\cos\varphi + j\sin\varphi) \\ j\cos\varphi - \sin\varphi \end{pmatrix} \cdot \begin{pmatrix} \vec{e}_r \\ \vec{e}_\theta \\ \vec{e}_\varphi \end{pmatrix}. \tag{2}$$

Therefore, the magnetic flux density can be reformulated as

$$\vec{B}_0 = \mathrm{Re}\{B_0 \, \vec{b} \, e^{j\omega t}\}. \tag{3}$$
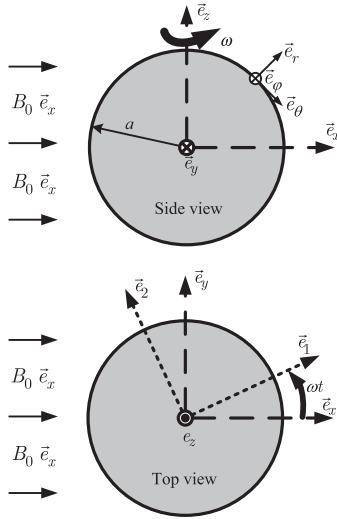
FIG. 1. Fixed Cartesian $(\vec{e}_x \quad \vec{e}_y \quad \vec{e}_z)^{\mathrm{T}}$, rotating Cartesian $(\vec{e}_1 \quad \vec{e}_2 \quad \vec{e}_z)^{\mathrm{T}}$, and rotating spherical $(\vec{e}_r \quad \vec{e}_\theta \quad \vec{e}_\varphi)^{\mathrm{T}}$ coordinate systems. The ball spins in counterclockwise direction and is subject to a constant external magnetic flux density with amplitude B_0.

A. Basic equations

The electromagnetic field problem can be solved by calculating the vector potential $\vec{A}$, from which the remaining properties of interest can easily be derived.[8–10] The solution for $\vec{A}$ is found by considering basic equations and certain boundary conditions. The vector potential is linked with the magnetic flux density $\vec{B}$ through

$$\vec{\nabla} \times \vec{A} = \vec{B}, \tag{4}$$

where $\vec{\nabla}$ is the Nabla operator. Additionally, the Coulomb gauge[11] is chosen for this problem, which results in

$$\vec{\nabla} \cdot \vec{A} = 0. \tag{5}$$

From the well-known relation between the electric field $\vec{E}$ and the magnetic flux density

$$\vec{\nabla} \times \vec{E} = -\frac{\partial \vec{B}}{\partial t}, \tag{6}$$

the relation between the electric field and the vector potential can be derived as

$$\vec{E} = -\frac{\partial \vec{A}}{\partial t}. \tag{7}$$

It has to be noted that there is no gradient of a scalar potential in Eq. (7) because there is no initial static charge on the sphere. Two additional well-known field equations are required. The first one links the magnetic flux density with the current density $\vec{J}$ and is written as

$$\vec{\nabla} \times \vec{B} = \mu_0 \, \mu_r \, \vec{J}, \tag{8}$$

where μ_0 is the vacuum permeability and μ_r is the relative permeability. The second field equation, which relates the current density with the electric field, consists of two parts, namely, the conductor based current and the displacement current. For the problem at hand, the latter can be neglected as the conductor based current is clearly dominant, resulting in

$$\vec{J} = \sigma \vec{E}, \tag{9}$$

with σ being the electrical conductivity. Combining Eqs. (4) and (7)–(9), the following fundamental equation for the vector potential can be found:

$$\vec{\nabla} \times (\vec{\nabla} \times \vec{A}) = -\mu_0 \, \mu_r \, \sigma \frac{\partial \vec{A}}{\partial t}. \tag{10}$$

This equation can be rewritten by employing the identity $\vec{\nabla} \times (\vec{\nabla} \times \vec{A}) = \vec{\nabla}(\vec{\nabla} \cdot \vec{A}) - \Delta \vec{A}$ (with Δ being the Laplace operator) and the condition in Eq. (5), resulting in

$$-\Delta \vec{A} + \mu_0 \, \mu_r \, \sigma \frac{\partial \vec{A}}{\partial t} = 0. \tag{11}$$

B. Boundary conditions

The calculation of the vector potential has to be divided into two areas: the region inside the sphere (with radius a) and the region around it. For the latter, Eq. (11) can be simplified to

$$\Delta \vec{A} = 0, \tag{12}$$

as the conductivity σ is zero outside the ball.

In order to find the correct solution for the vector potential, three boundary conditions have to be considered. First of all, the radial component of the magnetic flux density B_{rad} has to be steady at the surface of the sphere. The flux density component just outside the sphere is denoted as $B_{\mathrm{rad}}^{\mathrm{out}}$, whereas at the inner side of the surface the notation $B_{\mathrm{rad}}^{\mathrm{in}}$ is used. Then, the requirement for steadiness can be written as

$$B_{\mathrm{rad}}^{\mathrm{out}} - B_{\mathrm{rad}}^{\mathrm{in}} = 0. \tag{13}$$

A similar boundary condition can be written for the tangential component of the magnetic field, leading to

$$H_{\mathrm{tan}}^{\mathrm{out}} - H_{\mathrm{tan}}^{\mathrm{in}} = 0. \tag{14}$$

The third boundary condition has to be considered for the vector potential $\vec{A}_0$ far away from the sphere, where a homogeneous magnetic flux density is found that is not influenced by the ball. In that case, the vector potential is subject to an asymptotic condition, which is given by

$$\vec{A} \to \vec{A}_0 = \frac{1}{2} \vec{B}_0 \times \vec{r}. \tag{15}$$

The position vector $\vec{r}$ in Eq. (15) identifies the position in space and can be expressed in spherical coordinates as

$$\vec{r} = \begin{pmatrix} r \\ 0 \\ 0 \end{pmatrix} \cdot \begin{pmatrix} \vec{e}_r \\ \vec{e}_\theta \\ \vec{e}_\varphi \end{pmatrix}. \tag{16}$$

C. Vector potential

For the vector potential of the entire space, an ansatz according to

$$\vec{A} = \frac{1}{2} B_0 \mathrm{Re}\{F(r)\, \vec{b} \times \vec{r}\, e^{j\omega t}\} \tag{17}$$

is used, for which the function $F(r)$ has to be determined in such a way that the field condition in Eq. (11) and all the boundary conditions are satisfied. Using spherical coordinates, the vector potential can be written as

$$\vec{A} = \frac{1}{2} B_0\, r \mathrm{Re}\left\{ F(r) \begin{pmatrix} 0 \\ [j\cos\varphi - \sin\varphi] \\ -\cos\theta[\cos\varphi + j\sin\varphi] \end{pmatrix} \cdot \begin{pmatrix} \vec{e}_r \\ \vec{e}_\theta \\ \vec{e}_\varphi \end{pmatrix} e^{j\omega t}\right\}. \tag{18}$$

By replacing the vector potential in the field condition of Eq. (11) with the ansatz from Eq. (18), the following differential equation can be found for the space inside the sphere:

$$\frac{\partial^2 F(r)}{\partial r^2} + \frac{4}{r}\frac{\partial F(r)}{\partial r} - j\mu\sigma\omega F(r) = 0, \tag{19}$$

for which the solution is given by

$$F(r) = c_1\left(\frac{\sin(c_{\mathrm{EC}}\, r)}{(c_{\mathrm{EC}}\, r)^3} - \frac{\cos(c_{\mathrm{EC}}\, r)}{(c_{\mathrm{EC}}\, r)^2}\right) = c_1 f(c_{\mathrm{EC}}\, r). \tag{20}$$

The integration constant c_1 will be determined through the boundary conditions. The so-called eddy current constant c_{EC} is defined as

$$c_{\mathrm{EC}} = \sqrt{-j\mu_0\mu_r\sigma\omega}. \tag{21}$$

In the vacuum around the spinning ball, the field condition from Eq. (12) is used, resulting in a simpler differential equation

$$\frac{\partial^2 F(r)}{\partial r^2} + \frac{4}{r}\frac{\partial F(r)}{\partial r} = 0. \tag{22}$$

The solution of Eq. (22) can be calculated to

$$F(r) = c_2 + c_3\frac{1}{r^3}, \tag{23}$$

with two additional integration constants.

From the first boundary condition in Eq. (13), the following relation can be derived:

$$F^{\mathrm{out}}(r \to a) - F^{\mathrm{in}}(r \to a) = 0. \tag{24}$$

This relation can be achieved by expanding the functions from Eqs. (20) and (23) to

$$F(r) = c_1'\frac{f(c_{\mathrm{EC}}\, r)}{f(c_{\mathrm{EC}}\, a)} \tag{25}$$

and

$$F(r) = c_2 + c_3'\left(\frac{a}{r}\right)^3, \tag{26}$$

respectively. Additionally, the relation

$$c_1' = c_2 + c_3' \tag{27}$$

has to hold true. From the asymptotic condition in Eq. (15), it follows that

$$F(r) \to 1 \tag{28}$$

for $r \gg a$. This allows to determine the integration constant c_2 to the value 1. Finally, the boundary condition from Eq. (14) has to be considered. It leads to another differential equation, which is given by

$$\frac{1}{\mu_0}\left(r\frac{\partial F^{\mathrm{out}}(r \to a)}{\partial r} + 2F^{\mathrm{out}}(r \to a)\right)$$
$$- \frac{1}{\mu_0\mu_r}\left(r\frac{\partial F^{\mathrm{in}}(r \to a)}{\partial r} + 2F^{\mathrm{in}}(r \to a)\right) = 0. \tag{29}$$

From this equation, the integration constant c_3' can be derived as

$$c_3' = D(c_{\mathrm{EC}}\, a) = \frac{(2\mu_r + 1)g(c_{\mathrm{EC}}\, a) - 1}{(\mu_r - 1)g(c_{\mathrm{EC}}\, a) + 1}, \tag{30}$$

with an additional function defined as

$$g(c_{\mathrm{EC}}\, a) = f(c_{\mathrm{EC}}\, a)\frac{c_{\mathrm{EC}}\, a}{\sin(c_{\mathrm{EC}}\, a)} = \frac{1 - (c_{\mathrm{EC}}\, a)\cot(c_{\mathrm{EC}}\, a)}{(c_{\mathrm{EC}}\, a)^2}. \tag{31}$$

Finally, the complete solution for $F(r)$ becomes

$$F(r) = [1 + D(c_{\mathrm{EC}}\, a)]\frac{f(c_{\mathrm{EC}}\, r)}{f(c_{\mathrm{EC}}\, a)} \tag{32}$$

for the region inside the sphere with $r \le a$ and

$$F(r) = 1 + D(c_{\mathrm{EC}}\, a)\left(\frac{a}{r}\right)^3 \tag{33}$$

for the region outside the sphere (vacuum) with $r > a$.

D. Magnetic flux density

Once the vector potential is determined, the magnetic flux density can be calculated by employing Eq. (4), resulting in
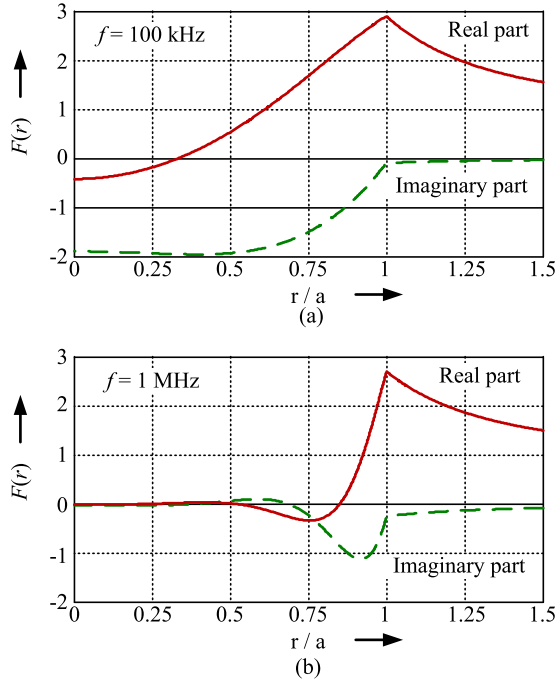
FIG. 2. Real and imaginary part of the amplifying function $F(r)$. For increased frequency, the amplification becomes more pronounced towards the ball surface. The physical parameters are set according to Table I.

$$\vec{B} = B_0 \text{Re} \left\{ \left[F(r) \begin{pmatrix} \sin\theta[\cos\varphi + j\sin\varphi] \\ \cos\theta[\cos\varphi + j\sin\varphi] \\ [j\cos\varphi - \sin\varphi] \end{pmatrix} \right. \right.$$
$$\left. \left. + \frac{r}{2} \frac{\partial F(r)}{\partial r} \begin{pmatrix} 0 \\ \cos\theta \cdot [\cos\varphi + j\sin\varphi] \\ [j\cos\varphi - \sin\varphi] \end{pmatrix} \right] \cdot \begin{pmatrix} \vec{e}_r \\ \vec{e}_\theta \\ \vec{e}_\varphi \end{pmatrix} e^{j\omega t} \right\}.$$
(34)

It can be seen that the magnetic flux density depends on the external homogenous flux density B_0. Due to the influence of the spinning ball, an amplification of the magnetic flux density can be observed, which is expressed with the characteristic function $F(r)$ as well as its derivative. These two functions are plotted in Figs. 2 and 3, respectively, for two different rotational frequency values. The figures reveal that the flux density is amplified in dependence on the radial distance from the ball center. For increasing frequency, the amplification becomes more dominant in the region of the ball surface. Moreover, the derivative part from Fig. 3 clearly outweighs the function in Fig. 2 for the higher frequency.
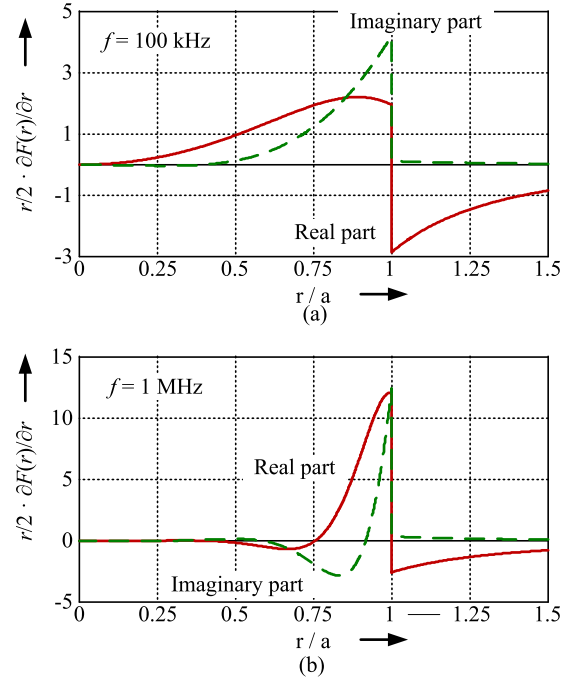
FIG. 3. Real and imaginary part of the derivative of the amplifying function $F(r)$, multiplied with r/2. For increased frequency, the amplification becomes more pronounced towards the ball surface, and, additionally, the influence of the derivative clearly outweighs the influence of $F(r)$ from Fig. 2. The physical parameters are set according to Table I.

In the middle of the sphere, cut by the x-y-0-plane, the flux density distribution can be simplified to

$$\vec{B} = B_0 \text{Re} \left\{ \left[F(r) \begin{pmatrix} [\cos\varphi + j\sin\varphi] \\ 0 \\ [j\cos\varphi - \sin\varphi] \end{pmatrix} \right. \right.$$
$$\left. \left. + \frac{r}{2} \frac{\partial F(r)}{\partial r} \begin{pmatrix} 0 \\ 0 \\ [j\cos\varphi - \sin\varphi] \end{pmatrix} \right] \cdot \begin{pmatrix} \vec{e}_r \\ \vec{e}_\theta \\ \vec{e}_\varphi \end{pmatrix} e^{j\omega t} \right\}. \quad (35)$$

Hence, the direction of the flux density is aligned with the plane, as will be further shown in Sec. III.

E. Current density

The current density inside the sphere can be derived from the vector potential as well. Combining Eqs. (7) and (9) leads to

$$\vec{J} = -\sigma \frac{\partial \vec{A}}{\partial t} = -\frac{1}{2} B_0 \sigma \omega r \text{Re} \left\{ F(r) \cdot \begin{pmatrix} 0 \\ [-\cos\varphi - j\sin\varphi] \\ -\cos\theta[j\cos\varphi - \sin\varphi] \end{pmatrix} \cdot \begin{pmatrix} \vec{e}_r \\ \vec{e}_\theta \\ \vec{e}_\varphi \end{pmatrix} e^{j\omega t} \right\}. \quad (36)$$

Outside the sphere, the current density is zero as there is zero conductivity in vacuum.

As before, the distribution in the middle of the sphere, cut by the x-y-0-plane, is considered exemplarily. For the current density, only one direction remains:

$$\vec{J} = -\frac{1}{2} B_0 \sigma \omega r \text{Re}\{F(r)[-\cos\varphi - j\sin\varphi]\vec{e}_\theta e^{j\omega t}\}. \quad (37)$$

The current density direction is perpendicular to the x-y-0-plane, pointing into the positive or negative z-direction.

In fact, the current distribution consists of loops inside the ball, as will be further demonstrated in Sec. III.

F. Torque

The torque per volume can be found as the cross product of the radius and the force per volume inside the sphere, denoted as

$$d\vec{T} = \vec{r} \times d\vec{F}. \tag{38}$$

The force per volume itself is the cross product of the current density and the magnetic flux density, wherefore the torque per volume becomes

$$d\vec{T} = \vec{r} \times (\vec{J} \times \vec{B}). \tag{39}$$

Finally, the total motor torque can be found by integrating the torque per volume over the whole spinning ball. For the spherical coordinate system used, this integration is given by

$$\vec{T} = \int_0^{2\pi} \int_0^{\pi} \int_0^{r} \vec{r} \times (\vec{J} \times \vec{B}) r^2 \sin\theta \, dr \, d\theta \, d\varphi. \tag{40}$$

As a more elegant alternative to evaluating the integral in Eq. (40), the torque can be calculated by considering the spinning ball as a magnetic dipole $\vec{m}$, which is related to the vector potential through

$$\vec{A} = \frac{\mu_0}{4\pi} \frac{\vec{m} \times \vec{r}}{r^3}. \tag{41}$$

For the considered sphere radius a, the magnetic dipole can then be written as

$$\vec{m} = \frac{2\pi}{\mu_0} a^3 B_0 \mathrm{Re} \left\{ F(a) \begin{pmatrix} 1 \\ j \\ 0 \end{pmatrix} \cdot \begin{pmatrix} \vec{e}_x \\ \vec{e}_y \\ \vec{e}_z \end{pmatrix} \right\}. \tag{42}$$

The motor torque can be found as the cross product of the magnetic dipole and the external homogenous magnetic flux density ($\vec{T} = \vec{m} \times \vec{B}_0$), resulting in

$$\vec{T} = -B_0 m_y \vec{e}_z. \tag{43}$$

This second calculation method is advantageous as the external magnetic flux density B_0 is independent of the variable r and constant. Through evaluation of Eqs. (42) and (43), the torque can be reformulated to

$$\vec{T} = \underbrace{\frac{3\pi a^3}{1 + \sqrt{2}} \frac{B_0^2}{\mu_0}}_{T_{bd}} \frac{2 + \sqrt{2}}{\sqrt{2} + q + \frac{1}{q}} \vec{e}_z, \tag{44}$$

where the variable q stands for

$$q = \frac{1}{a} \sqrt{\frac{\mu_r}{\mu_0 \sigma \omega}}. \tag{45}$$

Additionally, the breakdown torque T_{bd} has been marked in Eq. (44). It occurs at the angular frequency for which q in Eq. (45) becomes unity, which is the case if

$$\omega_{bd} = \frac{1}{a^2} \frac{\mu_r}{\mu_0 \, \sigma} = 2\pi f_{bd}. \tag{46}$$

The breakdown torque only depends on the amplitude of the homogenous magnetic flux density and the sphere radius. In particular, its value is independent of the angular frequency, the relative permeability, and the conductivity of the spinning ball.

For small angular frequencies, the motor torque can be approximated with

$$\omega \ll \omega_{bd}: \quad T \approx c_T B_0^2 a^4 \frac{\sqrt{\omega}}{\sqrt{\mu_r}}, \tag{47}$$

employing a torque constant c_T, whereas for large angular frequencies the motor torque is approximated with

$$\omega \gg \omega_{bd}: \quad T \approx c_T B_0^2 a^2 \frac{\sqrt{\mu_r}}{\sqrt{\omega}}. \tag{48}$$

Hence, over the whole frequency range, the torque depends in a quadratic relation on the amplitude of the magnetic flux density. Moreover, in the targeted range below the breakdown torque, the ball radius influences the torque with a factor to the power of 4.

The motor torque characteristics for such a solid rotor induction machine are presented in Fig. 4. The torque has been normalized with the breakdown torque, whereas the angular frequency has been normalized with the breakdown frequency. Due to this normalization of both axes, the shape of the torque curve in Fig. 4 becomes completely independent of all the aforementioned physical parameters. According to Eqs. (47) and (48), the torque curve increases approximately proportionally to $\sqrt{\omega}$ for small frequencies and decreases approximately proportionally with $1/\sqrt{\omega}$ for larger frequencies beyond the breakdown torque.
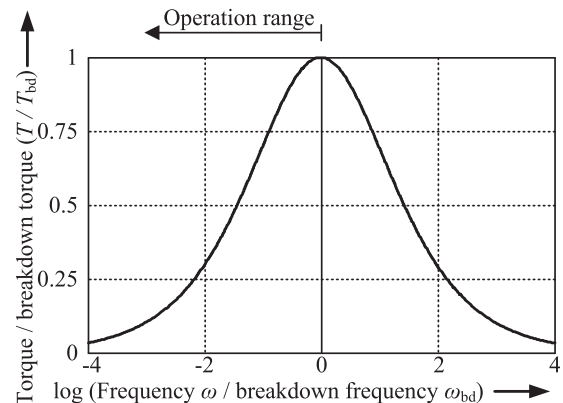
FIG. 4. Motor torque (normalized with the breakdown torque) in relation to the angular frequency (normalized with the breakdown frequency).
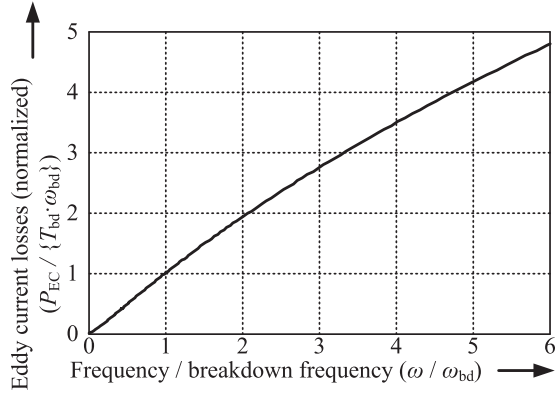
FIG. 5. Eddy current losses (normalized with the motor power at breakdown torque) in relation to the frequency (normalized with the breakdown frequency).

G. Eddy current losses

The ohmic loss density due to the eddy currents can be expressed as

$$p_{EC} = \frac{1}{\sigma}\vec{J}^2. \tag{49}$$

As before for the torque, the overall losses result from an integration of the loss density over the entire volume of the spinning ball, written in spherical coordinates as

$$P_{EC} = \int_0^{2\pi}\int_0^{\pi}\int_0^{r} \frac{1}{\sigma}\vec{J}^2 r^2 \sin\theta \, dr \, d\theta \, d\varphi. \tag{50}$$

Given that the hysteresis losses in the spinning ball have been neglected (which is justified for the high rotational speeds, as the eddy current losses are clearly dominant com-

TABLE I. Parameter of motor setup used for comparison.

Name	Symbol	Value
Rotor radius	r_R	0.5 mm
Magnetic flux density	B_0	10 mT
Conductivity of steel ball	σ	10^6 S/m
Relative permeability of steel ball	μ_r	100
Conductivity of environment	σ	0 S/m
Relative permeability of environment	μ_r	1
Relative permittivity	ε_r	1

pared to the hysteresis losses[12]), the eddy current losses are equal to the motor power and can easily be calculated with

$$P_{EC} = P_M = T\omega. \tag{51}$$

In reality, additional losses such as air friction losses,[13] iron and copper losses in the stator,[14,15] and losses in the power electronic converter[16] have to be considered, too, which lower the efficiency of the motor.

Fig. 5 shows the characteristics of the eddy current losses. These losses have been normalized with the motor power at breakdown torque (as the product of the breakdown torque and the angular breakdown frequency). The frequency itself has also been normalized with the breakdown frequency. Despite the breakdown in torque, the losses steadily increase with the angular frequency.

III. COMPARISON WITH 3D FINITE ELEMENT ANALYSIS

In order to validate the theoretical model, a comparison with 3D finite element simulations is drawn. For this comparison, a realistic scenario is chosen, with the employed parameters given in Table I.
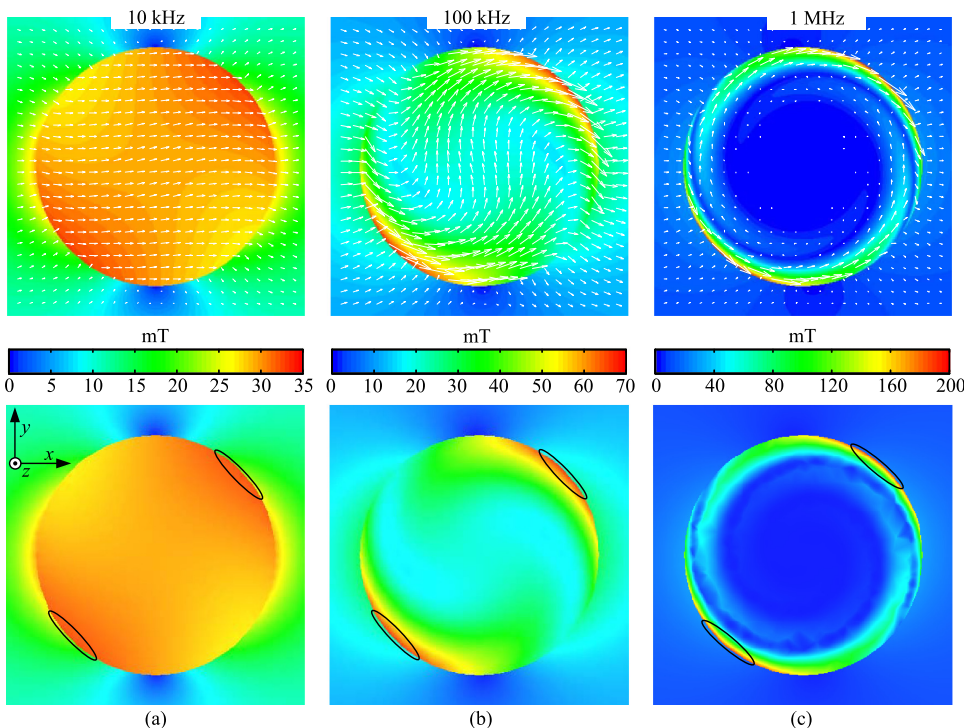
FIG. 6. Graphical plot of the amplitude of the magnetic flux density inside the sphere cut through the x-y-plane at $z = 0$ at the moment when the two Cartesian coordinate systems are aligned. Three different rotational frequencies of (a) 10, (b) 100, and (c) 1000 kHz are shown. The upper plots result from the theoretical calculations, whereas the lower plots are derived from the 3D finite element simulations. Additionally, the direction of the flux density has been marked in the upper plots.
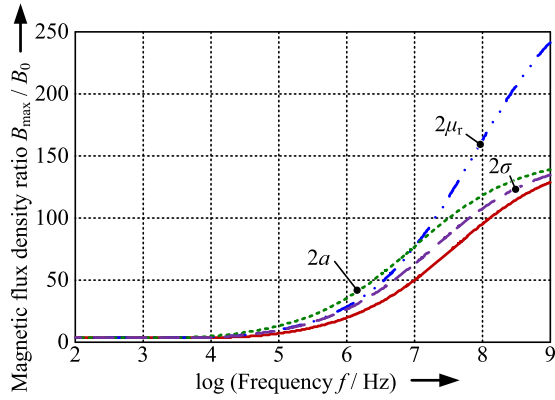
FIG. 7. Maximum magnetic flux density at the border of the steel ball (normalized with the homogenous magnetic flux density of the environment) in dependence on the rotational frequency.

A. Magnetic flux density

From the theoretical analysis, the magnetic flux density has been derived in Eq. (34). In the upper row of Fig. 6, the amplitude of this flux density is plotted inside the sphere for three different rotational frequencies with the ball spinning in counterclockwise direction. The spheres have been cut through the middle in the x-y-plane for $z = 0$, corresponding to the scheme in the lower plot of Fig. 1. Moreover, the two Cartesian coordinate systems are aligned. In the lower row of Fig. 6, the corresponding plots resulting from 3D finite element simulations have been added. A convincing similarity in color and shape of the flux density pattern can be found for all three frequencies. Moreover, the direction of the flux density has been marked in the upper plot, resulting directly from the simplified equation found in Eq. (35).

Fig. 6 also reveals that the increase in magnetic flux density is more pronounced towards the surface of the sphere for increasing rotational frequencies. Therefore, the maximum increase in the amplitude of the magnetic flux density (related to the homogeneous flux density with amplitude B_0) has been investigated and is plotted in Fig. 7 (solid line).

In the targeted region up to 10^8 Hz (see further down), an increase with factor 100 can be observed, which, for the chosen values, would correspond to 1 T. Both the analytical model and the simulations are based on a constant relative permeability, which differs from the hysteresis characteristic of a real material. Nevertheless, as the material does not saturate (except for a possible small area close to the surface), such an approximation with a constant value can be justified.

Fig. 7 further reveals the influence of doubling a certain physical parameter. Interestingly, doubling either the ball radius or the conductivity only slightly increases the maximum magnetic flux density found within the sphere. However, an increase in the relative permeability could quickly result in a maximum flux density beyond the saturation level of the material, in which case the simplification with linear material cannot be upheld anymore. Hence, the model validity has to be checked for each setup in dependence on the actual physical parameters.

B. Current density

In a similar manner than before for the magnetic flux density, the amplitude of the current density has been compared between the result from the theoretical analysis Eq. (36) and 3D finite element simulations. The upper row in Fig. 8 shows the outcome resulting from the theoretical considerations, and the comparison with the simulated results in the lower row reveals a convincing similarity, too. A more pronounced increase of the current density towards the surface of the sphere can be observed as well.
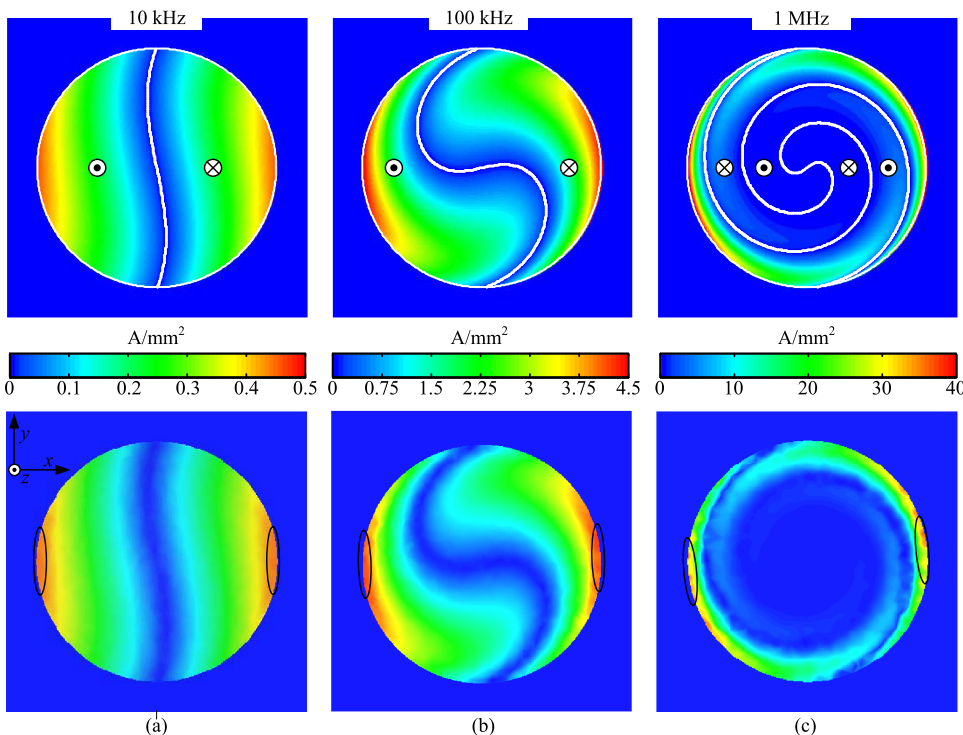
FIG. 8. Graphical plot of the amplitude of the current density inside the sphere cut through the x-y-plane at $z = 0$ at the moment when the two Cartesian coordinate systems are aligned. Three different rotational frequencies of (a) 10, (b) 100 and (c) 1000 kHz are shown. The upper plots result from the theoretical calculations, whereas the lower plots are derived from the 3D finite element simulations. Additionally, the pointing direction of the current density has been marked in the upper plots.
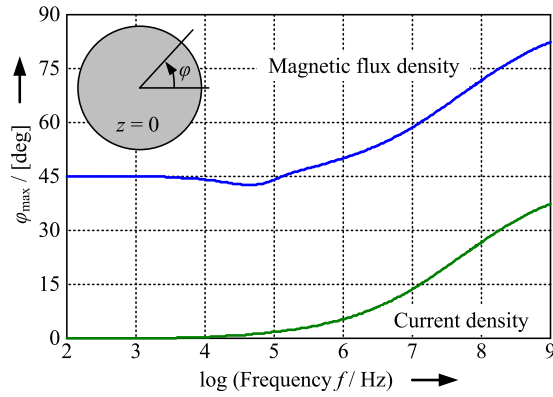
FIG. 9. Angle of the maximum magnetic flux density and the maximum current density in dependence on the rotational frequency.

As mentioned in Sec. II, the current density points into the z-direction for the x-y-0-plane considered. Therefore, the actual direction is marked in the upper plots of Fig. 8. The current describes loops, which overlap each other with increasing rotational frequency.

For both the magnetic flux density and the current density, a rotational pattern can be found for the amplitude. In Fig. 9, the angle of the maximum amplitude for both physical quantities is given in dependence on the rotational frequency. It can be seen that there is an increase in the angle for rotational speeds beyond 10^5 Hz. Additionally, Fig. 9 reveals that there is a permanent phase difference in the range of $45°$ between the amplitude maxima of magnetic flux density and current density. The maxima of both the magnetic flux density and the current density have been marked with circles in the lower plots of Figs. 6 and 8.

C. Torque

The torque characteristic of the spinning ball with the parameters from Table I is presented in Fig. 10. The solid line corresponds with the theoretical value calculated in Eq. (44), revealing a breakdown frequency of 50 MHz. Additionally, the torque calculated from the 3D finite element analysis is represented with blue circles. For the frequency range of 10^5 to 10^8 Hz, a very good alignment can be found that clearly confirms the theoretical results. The small difference for the lower frequency range can be explained with the upper limit
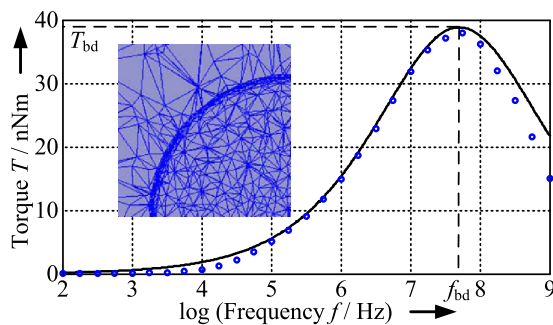
FIG. 10. Motor torque in dependence on the rotational frequency resulting from theoretical calculations (solid line) and from 3D FE simulations (circles). Moreover, the mesh of the simulation in the upper left quarter of the sphere is shown.

of the mesh resolution (the upper left quarter of the ball mesh has been added to Fig. 10) in case of the finite element analysis. In the most accurate range (10^5–10^8 Hz), the torque is mainly created in the sphere volume close to the surface, for which the mesh is extremely detailed. Beyond 10^8 Hz, an even more detailed mesh close to the surface would be required to accurately predict the torque trough simulations.

IV. CONCLUSIONS

An analytical solution has been derived for a rotating sphere in a homogenous magnetic field. It gives the foundation to accurately determine the magnetic flux density and the current density characteristics of a prototype setup employed for a world record attempt. Additionally, integral values such as torque and eddy current losses can easily be derived. The validity of the theoretical analysis has been confirmed by means of comparison with a 3D finite element analysis. Through comparison of torque values as well as graphical comparisons of the amplitude of the magnetic flux density and the current density, the correctness of the theoretical solution has been proven.

The presented model builds the analytical basis for a future design of the ultra-high speed spinning ball setup.

ACKNOWLEDGMENTS

[1]J. W. Beams, J. L. Young, and J. W. Moore, "The production of high centrifugal fields," J. Appl. Phys. **17**, 886 (1946).

[2]B. E. Kane, "Levitated spinning graphene flakes in an electric quadrupole ion trap," Phys. Rev. B **82**, 115441 (2010).

[3]C. Wildmann, T. Nussbaumer, and J. W. Kolar, "Design considerations for the drive system of an ultra-high speed spinning ball motor," in Proceedings of the 2010 International Symposium on Power Electronics Electrical Drives Automation and Motion (SPEEDAM), Pisa, Italy, 14–16 June 2010, pp. 1478–1483.

[4]C. Wildmann, T. Nussbaumer, and J. W. Kolar, "10 Mrpm spinning ball motor: Preparing the next generation of ultra-high speed drive systems," in Proceedings of the 2010 International Power Electronics Conference (IPEC), Sapporo, Japan, 21–24 June 2010, pp. 278–283.

[5]Y. Hu, J. Chen, and X. Ding, "Analysis and computation on magnetic field of solid rotor induction motor," IEEE Trans. Appl. Supercond. **20**, 1844 (2010).

[6]J. F. Gieras and J. Saari, "Performance calculation for a high-speed solid-rotor induction motor," IEEE Trans. Ind. Electron. **59**, 2689 (2012).

[7]E. Dlala and A. Arkkio, "Measurement and analysis of hysteresis torque in a high-speed induction machine," IET Electric Power Appl. **1**, 737 (2007).

[8]J.-Y. Choi and S.-M. Jang, "Analytical magnetic torque calculations and experimental testing of radial flux permanent magnet-type eddy current brakes," J. Appl. Phys. **111**, 07E712 (2012).

[9]S.-M. Jang, H.-K. Kim, J.-Y. Choi, and K.-J. Ko, "Analysis and comparison for rotor eddy current losses of permanent magnet synchronous generator according to dc and ac load conditions," J. Appl. Phys. **105**, 07F109 (2009).

[10]J. W. Jansen, E. A. Lomonova, and J. M. M. Rovers, "Effects of eddy currents due to a vacuum chamber wall in the airgap of a moving-magnet linear actuator," J. Appl. Phys. **105**, 07F111 (2009).

[11]D. M. Drury, "The unification of the Lorentz and Coulomb gauges of electromagnetic theory," IEEE Trans. Educ. **43**, 69 (2000).

[12]K. Yamazaki, A. Suzuki, M. Ohto, and T. Takakura, "Harmonic loss and torque analysis of high-speed induction motors," IEEE Trans. Ind. Appl. **48**, 933 (2012).

[13]J. Luomi, C. Zwyssig, A. Losser, and J. W. Kolar, "Efficiency optimization of a 100-W 500 000-r/min permanent-magnet machine including air-friction losses," IEEE Trans. Ind. Appl. **45**, 1368 (2009).

[14]K. Komeza and M. Dems, "Finite-element and analytical calculations of no-load core losses in energy-saving induction motors," IEEE Trans. Ind. Electron. **59**, 2934 (2012).

[15]L. Dupré, P. Sergeant, and L. Vandenbossche, "Magnetic network model including loss separation and Preisach principles for the evaluation of core losses in devices," J. Appl. Phys. **97**, 10E515 (2005).

[16]L. Aarniovuori, L. I. E. Laurila, M. Niemelä, and J. J. Pyrhönen, "Measurements and simulations of DTC voltage source converter and induction motor losses," IEEE Trans. Ind. Electron. **59**, 2277 (2012).